J. Phys. D: Appl. Phys. **33** (2000) R157–R172. Printed in the UK PII: S0022-3727(00)13775-1

REVIEW ARTICLE

Controlling the properties of high energy density permanent magnetic materials by different processing routes

O Gutfleisch

Institute of Solid State and Materials Research Dresden, PO Box 270016, 01171 Dresden, Germany

E-mail: o.gutfleisch@ifw-dresden.de

Received 8 May 2000

Abstract. This article addresses the most recent developments in the processing of high-performance magnets based on rare earth–transition metal (R–T) compounds. It gives an overview of the relevant classes of R–T compounds together with a description of the appropriate manufacturing route and an assessment of their potential for application. The paper pays particular attention to state-of-the-art maximum energy density and high-temperature magnets as well as to the synthesis of nanostructured materials using non-equilibrium techniques and reversible hydrogen-induced phase transformations. The possibilities of increasing the energy density of the nanocrystalline magnets by remanence enhancement utilizing intergranular exchange coupling, by texturation via hot deformation or by hydrogenation disproportionation desorption and recombination to produce anisotropic powders are discussed.

1. Introduction

Permanent magnet materials are key components of numerous electronic (e.g. portable audio/video), data processing (e.g. voice coil motors (VCMs)) and medical devices (e.g. magnetic resonance imaging (MRI)) and significant amounts are needed in the automotive industry (e.g. eddy current breaking (ECB)). The annual growth rates in production are more than 10%. Despite being used for more than one thousand years, a boom only occurred in the mid-1960s with the development of rare earth permanent magnets (RPMs) based on intermetallic compounds of rare earths (Rs) and the transition metals (Ts) Fe or Co [1]. The auspicious combination of properties of the R sublattice (4f) and the T sublattice (3d) led to the spectacular development in the energy density, or also energy product, $(BH)_{max}$ of hard magnetic materials, as illustrated in figure 1. The former provides the high magnetic anisotropy, the latter the high Curie temperature and magnetization. The maximum energy density of RPMs, a measure of the magnetostatic energy stored, is limited by their remanence or remanent polarization J_r according to equation (1), provided the coercivity has at least half the value of the remanence:

$$(BH)_{max} = J_r^2/4\mu_0 \tag{1}$$

where μ_0 is the permeability of free space. J_r is half of the saturation polarization J_s for an assembly of isotropic non-interacting single domain particles (or more generally for textured magnets: $J_r \leqslant J_s$). $(BH)_{max}$ has doubled every 12 years during the 20th century with the progress being made due to improvements in coercivity, H_c, and not in magnetization, M_s (with $J_s = \mu_0 M_s$). The coercivity is usually described by

$$H_c = \frac{2K_1}{J_s}\alpha - N_{eff}\frac{J_s}{\mu_0} \tag{2}$$

where K_1 (assuming $K_1 \geqslant K_2$) is the anisotropy constant and α and N_{eff} are microstructural parameters, the former describing the reduction of the crystal field by defects as well as by misaligned grains and the latter taking into account internal stray fields [2, 3]. In practice however, coercivities of only 20–30% of the theoretical maximum, the anisotropy field, H_A (with $H_A = 2K_1/J_s$) are realized which can be explained by the existence of inhomogeneities with spatial variations in the anisotropy in real systems. This is known as Brown's paradox [4].

Section 2 gives a brief overview of the rare earth–transition metal magnet materials which are currently under scrutiny in the research community. The reader can thus grasp the variety of the different classes of R–T compounds and of their intrinsic properties.

0022-3727/00/170157+16$30.00

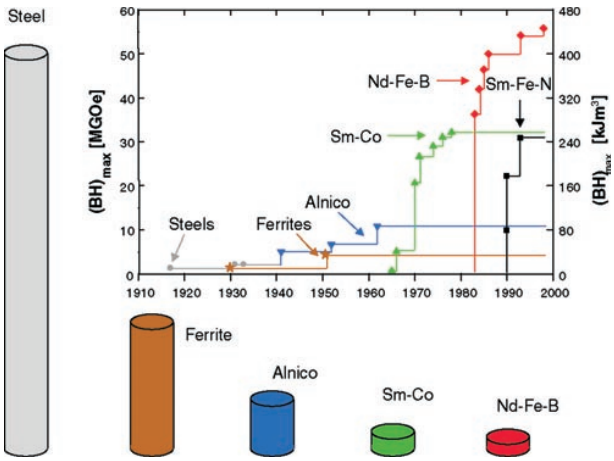

Figure 1. Development in the energy density $(BH)_{max}$ of hard magnetic materials in the 20th century and presentation of different types of materials with comparable energy densities.

Section 3 describes the complex task of transferring the intrinsic properties into extrinsic properties by appropriate processing. Microstructures with energy barriers preserving the metastable, permanently magnetized state need to be developed so that useful remanences and coercivities across a large temperature range arise. The different manufacturing routes for high-energy-density RPMs are reviewed with particular emphasis being placed on their limitations with respect to the physical properties and thermal stabilities of the micro- and nanocrystalline materials. The first part is devoted to maximum energy density magnets based on Nd–Fe–B (including a brief reference to their corrosion behaviour) and to recent developments in the field of high-temperature magnets based on Sm–Co, which become more and more relevant as RPMs are used in devices which operate at high temperatures. The different preparation methods to obtain the nanoscale structures such as non-equilibrium and hydrogen assisted processing routes as well as the important group of interstitially modified compounds are described in the following section. Finally, concepts of maximizing the energy product in nanostructured magnets by either inducing a texture via HDDR (hydrogenation disproportionation desorption and recombination) processing or hot deformation or enhancing the remanence via exchange coupling are reviewed. The paper ends with a short summary and outlook.

2. R–T magnetic materials

The search for new compounds with superior properties focuses on materials with high values of the Curie temperature ($T_C > 500$ K), high saturation magnetization ($M_s > 1$ T) and high anisotropy field, H_A. These intrinsic properties depend on the crystal structure and chemical composition and a favourable combination of these values does not lead automatically to a good hard magnetic material, but can only be regarded as a prerequisite. The final suitability can only be assessed when the extrinsic properties such as the coercive field H_C, remanent magnetization B_r and maximum energy product $(BH)_{max}$, derived from the intrinsic properties by the preparation of adequate

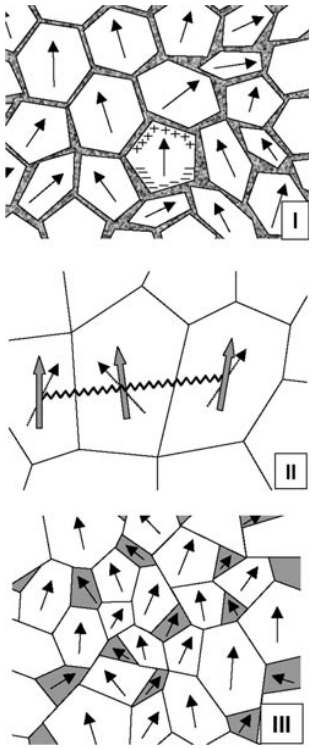

Figure 2. Three prototypes of RPMs based on $Nd_2Fe_{14}B$ with idealized microstructures. Type (I) is R rich and the individual crystallites are separated by a thin paramagnetic layer (grey). Long-range dipolar interaction is dominant and each hard magnetic grain behaves like a small permanent magnet, which results in high coercivities. The grains in type (II) are based on stoichiometric $Nd_2Fe_{14}B$ and are exchange coupled as no additional phase is present, leading to remanence enhancement. Type (III) is a nanocomposite magnet, where a Nd-deficient composition is used and the coupling occurs between the $Nd_2Fe_{14}B$ grains and soft magnetic Fe-rich grains (grey), resulting in a further increase in remanence.

microstructures, fulfil certain criteria. The intrinsic magnetic properties and micromagnetic parameters of the most important R–T compounds are summarized in table 1. Included are $Nd_2Fe_{14}B$- and SmCo-based compounds, which are currently the most relevant for applications, and also the other recently discovered hard magnetic iron-rich compounds such as $ThMn_{12}$-type compounds and the interstitial solid solutions of N and C in R_2Fe_{17}-type compounds. The domain wall width δ_w in hard magnets is comparable in size to the exchange length l_{ex} (see section 3.2.3), the latter describing the scale of the perturbed area when a spin is unfavourably aligned; whereas in soft magnets, $\delta_w \ll l_{ex}$ is valid. The critical single-domain particle size d_c describes the size of the largest possible crystallite in which the energy cost for the formation of a domain wall is higher than the gain in magnetostatic energy. Typical values for iron-based RPMs are of the order of 200–300 nm. There are two basic concepts for the prevention of nucleation and growth of reverse domains from the fully magnetized state (magnetization reversal): (a) for microcrystalline sintered magnets and (b) for single-domain grains found in nanostructured magnets obtained by melt spinning, mechanical alloying or HDDR. The former concept is realized firstly in the nucleation type, as found in sintered NdFeB-type magnets consisting of multi-

Table 1. The structure type, intrinsic magnetic properties (the Curie temperature T_C, the anisotropy field $H_A = (2K_1 + 4K_2)/J_s$, the anisotropy constant K_1, the saturation magnetization $\mu_0 M_S$, the upper limit of energy density $(BH)_{max} = \mu_0 M_S^2/4$), the domain wall width δ_w and the critical single-domain particle size d_c of important permanent magnet compounds and, for comparison, α-Fe and $F_{23}B_6$ (note: cubic structure) and Fe_3B (in-plane anisotropy). For further details the reader is referred to [21–23].

Compound	Structure type	T_C (K)	$\mu_0 H_A$ (T)	K_1 (MJ m^{-3})	$\mu_0 M_S$ (T)	$\mu_0 M_S^2/4$ (kJ m^{-3})	δ_w (nm)	d_c (μm)	Reference
$Nd_2Fe_{14}B$	Tetragonal $Nd_2Fe_{14}B$	585	6.7	5	1.60	516	4.2	0.3	[5, 6]
$Pr_2Fe_{14}B$	$Nd_2Fe_{14}B$	565	8.7	5	1.56	484	∼4	∼0.3	[7, 8]
$Nd_2Fe_{14}C$	$Nd_2Fe_{14}B$	532	9.5		1.41	396	∼4	∼0.3	[9, 10]
$SmCo_5$	Hexagonal $CaCu_5$	993	40	17	1.05	219	3.7	1.7	[11]
Sm_2Co_{17}	Rhombohedral Th_2Zn_{17}	1100	6.5	3.3	1.30	336	8.6	0.5	[11]
$Sm_2Fe_{17}N_3$	Th_2Zn_{17}	749	21	8.8	1.54	472	3.6	0.4	[12]
$Sm_2Fe_{17}C_3$	Th_2Zn_{17}	668	16	7.4	1.45	418		∼0.3	[12]
$Sm_3Fe_{26.7}V_{2.3}N_4$	Monoclinic $Nd_3(Fe,V)_{29}$	683	12		1.33	352		∼0.3	[13, 14]
$(Sm_{0.75}Zr_{0.25})Fe_{0.7}Co_{0.3})_{10}N_x$	Hexagonal $TbCu_7$	877	7.7		1.7	575		∼0.3	[15]
$NdFe_{10}V_2N_y$	Tetragonal $ThMn_{12}$	743	10		1.11	245		∼0.3	[16, 17]
$Sm(Fe_{11}Ti)$	$ThMn_{12}$	584	10.5	4.8	1.14	259	4.0	0.4	[18]
α-Fe	Bcc	1043		0.046	2.16	928	30	0.007	[19]
$Fe_{23}B_6$	Cubic	698		0.01	1.7				[19]
Fe_3B	Tetragonal	786	∼0.4	−0.32	1.62		20		[20]

domain grains in the thermally demagnetized, equilibrium state. Here the spontaneous nucleation of reverse domains is hindered by smooth grain boundaries, which also decouple the individual crystallites and thus impede propagation. Secondly, it is realized in the pinning type as found in sintered $Sm(Co_{bal}, Fe_w, Cu_x, Zr_y)_z$ magnets where the growth of reverse domains is prevented by pinning the existing domains at inclusions or defects. The nucleation and pinning type can be easily recognized from their respective virgin curve.

Figure 2 shows the three prototypes of RPMs based on $Nd_2Fe_{14}B$ with idealized microstructures. Type (I) is R rich and the individual crystallites are separated by a thin paramagnetic layer, the Nd-rich intergranular phase (see sections 3.1.1 and 3.5). This structure leads essentially to a magnetic decoupling and each hard magnetic grain behaves like a small permanent magnet, which results in high coercivities. Type (II) can be obtained using the stoichiometric $Nd_2Fe_{14}B$ composition and the grains are exchange coupled without an additional phase between them. As a consequence, a magnetic texture originates from the parallel alignment of the magnetic moment in the vicinity of the grain boundaries and provided the grains are small enough, a remanence enhancement is observed. A further increase in remanence is found in the type (III) nanocomposite magnets, a two- or multi-phase exchange coupled magnet, where a Nd-deficient composition (i.e. Nd concentrations less than 11.76 at.%) is used and the coupling occurs between the $Nd_2Fe_{14}B$ grains and the soft magnetic Fe-rich grains. The two latter types are described in more detail in section 3.2.3.

3. Processing routes

A review of the novel developments in the most relevant manufacturing routes, with special emphasis on nanostructured magnets, is given in the following sections. The flow chart of figure 3 illustrates the principal processing routes of RPMs. Each branch ends by machining and magnetizing the magnet. For the production of high-performance RPMs with maximum energy densities a careful control of low level metallic impurities such as Cu and non-metallic impurities such as oxygen is pivotal during all processing stages, regardless of which processing route is chosen.

3.1. Sintered magnets

3.1.1. Maximum energy density magnets. Anisotropic, sintered $Nd_2Fe_{14}B$-type magnets [6] with energy products $(BH)_{max}$ exceeding 400 kJ m^{-3} (50 MG Oe) are now produced routinely in industry (type (I) in figure 2). Conventional powder metallurgy is used, and generally the following requirements need to be fulfilled: a minimized oxygen content, a maximum volume fraction of the hard magnetic 2:14:1 phase with a commensurate reduction in the non-ferromagnetic grain boundary material, a small crystallite size with a narrow size distribution of typically 2–6 μm and a maximum alignment of the easy axis of magnetization of the crystallites [24–26].

Typically, NdFeB-based sintered magnets consist, according to the ternary phase diagram, of three equilibrium phases: the hard magnetic, tetragonal $Nd_2Fe_{14}B$ phase, the boride $Nd_{1+\varepsilon}Fe_4B_4$ and the low-melting-point Nd-rich phase. Depending on the type of the dopant material (either substituting for the R or the T) additional non-magnetic or soft magnetic phases are formed in the multicomponent system [27]. Because the compositions of recent high energy density magnets are close to stoichiometry, conventionally cast materials would contain a high proportion of Fe dendrites due to the peritectic nature of the formation of the $Nd_2Fe_{14}B$

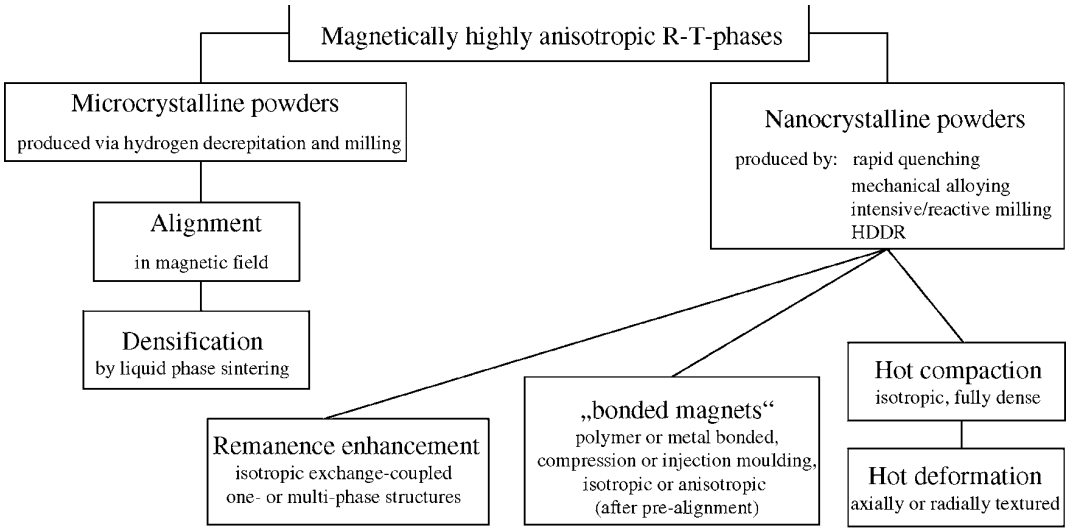

Figure 3. Flow chart illustrating the principal processing routes of high energy density RPMs based on micro- and nanocrystalline powders.

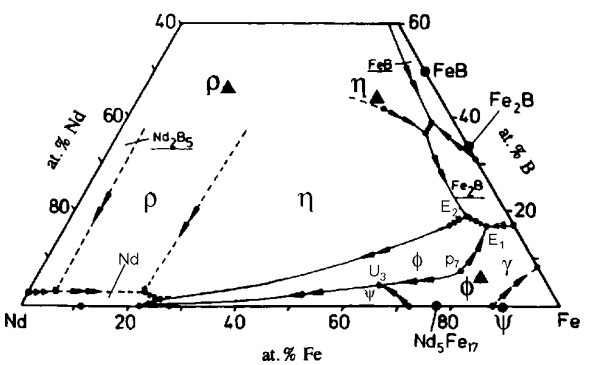

Figure 4. Liquidus projection of the Nd–Fe–B system. The important reactions are p_7 (1180 °C: L + γ-Fe → Φ), U_3 (1130 °C: L + γ-Fe → Φ + ψ (Nd_2Fe_{17})), e_4 (1115 °C: L → η + Φ), E_1 (1105 °C: L → Φ + γ-Fe + Fe_2B) and E_2 (1095 °C: L → η + Φ + Fe_2B) (after Knoch *et al* [28]).

phase. An instructive presentation of the ternary Nd–Fe–B system with low B concentrations is given in the liquidus projection (L-liquid) shown in figure 4 [28]. The full circles mark the binary phases, the triangles denote the above ternary phases and the important reactions are indicate by e, p, E, and U, which are elucidated in the figure caption. The Φ phase is located in a region where γ-Fe is the primary solidification product, i.e. in the pseudobinary phase diagram, with Nd:B = 2:1, the solidification path passes through the (L + Fe) region [29]. Fe is not only detrimental to the crushability during jet milling, but also to the magnetic properties of the magnet. The recently introduced 'strip casting' method [30] suppresses both the formation of free Fe and large pools of Nd-rich phase and leads to a fine grained microstructure that is very suitable for subsequent hydrogen decrepitation (HD [31]—see also section 3.3.1) and jet milling. The strip casting method consists of casting molten alloys onto a rotating water-cooled wheel, leading to the continuous formation of 0.3 mm thick flake-shaped ingots with grain sizes ranging from 5 to 60 μm, the larger ones close to the free surface side [32].

Pulverization is usually achieved by jet milling where an ultrasonic flow of inert gas induces mechanical collisions of the particles. During this process oxidation and particle welding have to be avoided, the former being detrimental to densification, the latter leading to misalignment. Milling in liquid media with low moisture and oxygen levels can be beneficial. A large magnetic torque, i.e. large magnetic fields well exceeding 1 MA m^{-1}, are necessary in order to achieve a maximum degree of alignment (see figure 5, from [33]). Mechanical friction is essential to hold the powder particles together when producing the green compact (porous body after predensification) and the packing density needs to be maximized in order to avoid particle relocation, leading to decreased alignment. Sagawa and Nagata [34] innovated the rubber isostatic pressing (RIP) technique in order to overcome these problems. Near net-shaped green compacts are produced using a thick rubber mould confined by a metallic die, the former creating a pseudo-hydraulic pressure. A comparison of the demagnetization curves of magnets manufactured by RIP and TDP (transverse die pressing) is shown in figure 6 (from [24]). A decreasing Nd content leads to increased B_r and $(BH)_{max}$ that is, however, accompanied by decreased coercivities. Careful control of the oxygen content is necessary because of the danger of forming Nd_2O_3 and resulting in densification problems. On the other hand, abnormal grain growth was observed for low oxygen contents, also lowering the magnetic properties [24].

In order to use the RPMs at elevated temperatures and to avoid irreversible flux losses, small temperature coefficients for remanence, $\alpha = (dM_r/dT)$, and coercivity, $\beta = (dH_c/dT)$, and good stability against corrosion [35, 36] are required. Generally, the coercivity and thus the temperature stability of Nd–Fe–B magnets is increased by a partial substitution of Nd by Dy [37]. However, the antiferromagnetic coupling between the Dy and Fe sublattices leads to a decreased saturation magnetization and thus remanence. Partial replacement of Fe by Co is used to minimize α and here the consequent loss in coercivity is compensated by the simultaneous addition of Ga, Al and Cu. The physical properties such as melting point and viscosity of

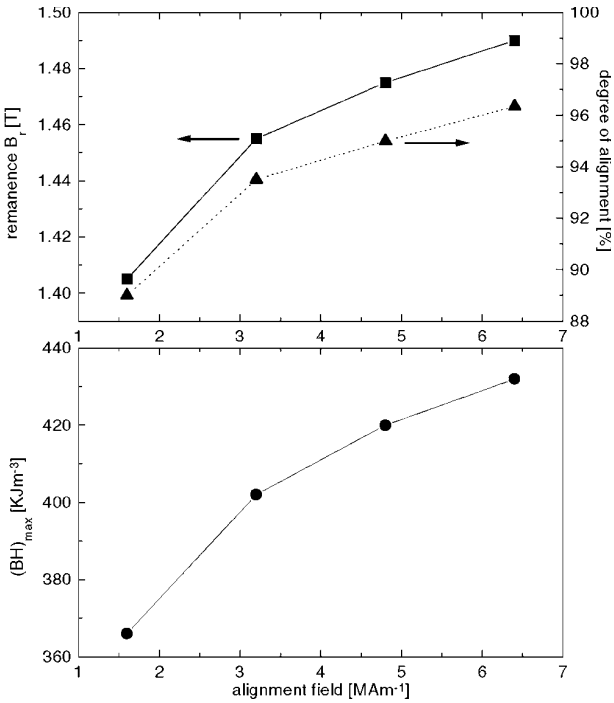

Figure 5. The effect of the magnetic alignment field on the remanence, the degree of alignment and $(BH)_{max}$ of the sintered high energy density NdFeB magnets (from Kaneko and Ishigaki [33]).

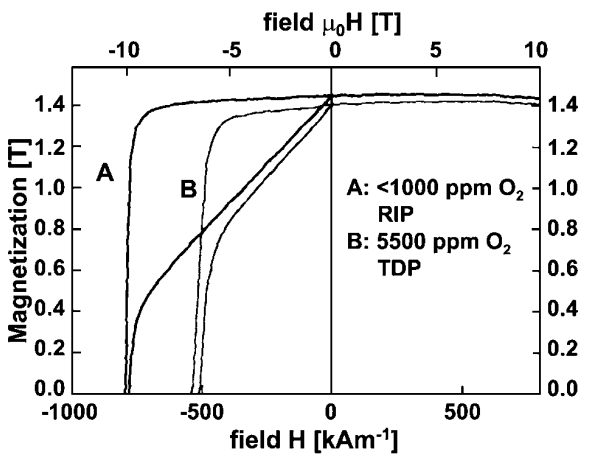

Figure 6. Comparison of demagnetization curves of $Nd_{13.5}Fe_{bal}B_{5.95}Cu_{0.03}Al_{0.7}$ sintered magnets manufactured by RIP and TDP: in air A, $(BH)_{max} = 50.2$ MG Oe and B, $(BH)_{max} = 41.9$ MG Oe (from Fidler *et al* [24]).

the intergranular phase depend sensitively on the composition and small amounts of additives. Ga addition, for example, can decrease the surface energy of this phase which leads to smoothed grain boundaries, and hence reduced R content, and improved corrosional properties. In warm and humid atmospheres, the Nd-rich intergranular phase in conventional Nd–Fe–B sintered magnets tends to form Nd hydroxides and some free hydrogen, which causes hydrogen embrittlement and therefore conventional magnets are usually coated. Another mechanism is electrolytic corrosion which occurs when water condenses on the magnet surface. In addition to encapsulation, the corrosional properties can also be improved by additions of Co, Cu, Al and Ga, their main effect is to transform the intergranular phases into more noble compounds [38].

3.1.2. High-temperature magnets. Microwave tubes, gyroscopes and accelerometers, reaction and momentum wheels to control and stabilize satellites, magnetic bearings, sensors and actuators are examples for applications where high energy density magnets with magnetic fields stable over a variety of environmental conditions and wide temperature ranges are required. $SmCo_5$- and Sm_2Co_{17}-type magnets [1, 11, 39, 40] are ideal for these applications because of their high magnetocrystalline anisotropies and Curie temperatures and they satisfy these requirements over the temperature range from 50 to 250 °C. In addition, they exhibit a high corrosion resistance, their disadvantages being the costly raw materials and difficult magnetization. A slight increase in the temperature stability can be achieved when substituting heavy R elements for Sm [41]. Even better temperature coefficients of remanence ($\alpha = (dM_r/dT)$) and coercivity ($\beta = (dH_c/dT)$) are required for higher operating temperatures such as 450 °C, which are needed for RPMs for electric vehicles, hybrid magnetic bearings for turbine engines and advanced power systems. The availability of these newly developed magnets could also open up completely new applications such as magnetic brakes with performance close to normal friction brakes.

Both the 1:5 and the 2:17 type are usually produced via the powder metallurgical sintering route. The latter one currently shows the best temperature coefficients α and β of all RPMs and its hard magnetic properties are achieved by an elaborate series of heat treatments, resulting in a complex microstructure. Commercially produced Sm–Co type sintered magnets based on the 2:17 phase have usually a composition close to $Sm(Co, Fe, Cu, Zr)_{7.5}$. The homogeneity region of the 2:17 phase narrows with decreasing temperature [42] and a fine cellular network of the $SmCo_5$ phase that is rich in Cu precipitates out from the single-phase metastable precursor obtained by solid solution treatment at about 1200 °C and quenching on the subsequent low-temperature annealing (∼800 °C). The cell interior (cell diameter ∼100 nm) with a rhombohedral 2:17 (Th_2Zn_{17} type) structure shows twin boundaries in the basal plane and a so-called 'platelet' or 'z phase' rich in Zr (2:17H, diameter 5–10 nm) is also observed parallel to the basal plane. The microstructure of a recent high-temperature, 2:17-type magnet is shown in the TEM image of figure 7. The rhombohedral structure can be derived from the $SmCo_5$ structure by an ordered substitution of a dumbbell of Co atoms for one-third of the Sm atoms. The subtle changes in microchemistry lead to a heterogeneous system in which the domain wall energy depends on the wall position and in which the walls remain pinned in regions where their energy is reduced. The gradient in Cu across the cell boundaries is facilitated by the presence of the Zr-rich lamellae and coincides with the gradient in the domain wall energy. This pinning type coercivity mechanism is responsible for the high coercivities in these solid-state precipitation hardened magnets.

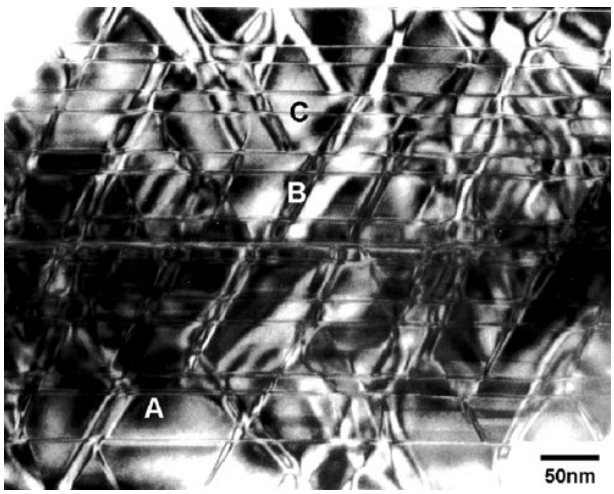

Figure 7. TEM bright field image of a high-temperature 2:17-based SmCo magnet (A denotes the 2:17 phase, B denotes the 1:5 phase and C denotes the Zr-rich phase) with ${}_JH_c = 600$ kA m^{-1} at 500 °C showing the typical cellular and lamellae structure (courtesy J Fidler, TU Vienna, Austria).

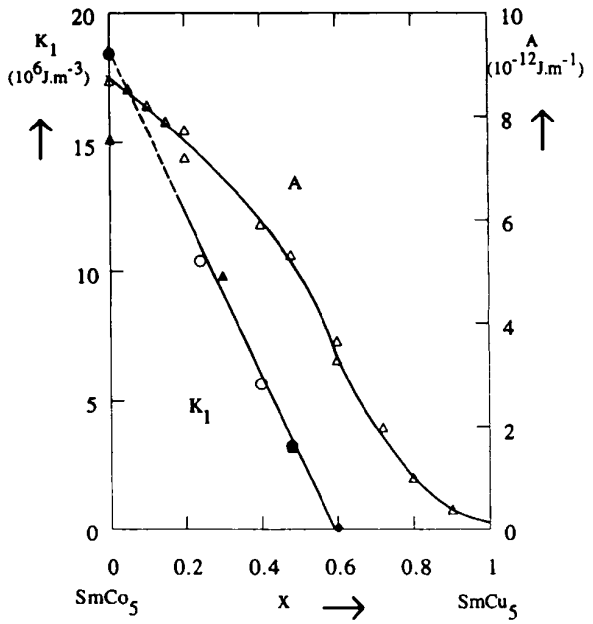

Figure 8. The anisotropy constant K_1 at 300 K and the exchange stiffness A against copper concentration of $Sm(Co_{1-x}Cu_x)_5$. K_1 shows a linear decrease with increasing Cu content (from Lectard *et al* [46]).

Due to the large variety in heat treatment and compositional parameters an optimization of the $Sm(Co_{bal}, Fe_w, Cu_x, Zr_y)_z$ magnets in terms of high-temperature magnetic properties is a complex task. Recent studies [43, 44] show that lower z values and higher amounts of Cu lead to a finer microstructure, which in turn results in a smaller temperature dependence of coercivity provided the appropriate Cu content is chosen. More specifically, it was shown that for $z \sim 8.5$ and $x = 0.088$ a room-temperature coercivity of 40 kOe was achieved, whereas for $z \sim 7$ and $x = 0.128$ a very high coercivity of 10.8 kOe at 500 °C was obtained. Further work showed that an increased Co content (lower Fe content) leads to maximum use temperatures of 400–550 °C. These magnets showed a straight demagnetization curve (B–H loop) in this temperature range, which is a requirement for dynamic applications [45]. Analytical electron microscopy showed that the Cu content in the $Sm(CoCu)_5$ cell boundary phase changes significantly and it was also reported that the anisotropy constant K_1 of this phase decreases dramatically with increasing Cu content, as shown in figure 8 [46], and is finally lower than that of the 2:17-type matrix phase. Consequently, a transition from attractive to repulsive pinning should be expected with increasing Cu content.

Nanocrystalline magnets of the $SmCo_5$, Sm_2Co_{17} and $PrCo_5$ types have been under scrutiny recently as they are also promising candidates for RPMs for high-temperature applications and they will be discussed in the later sections (3.2.1, 3.2.2 and 3.3.2).

3.2. Nanocrystalline magnets

3.2.1. Rapidly quenched magnets. The development of melt-spun or rapidly quenched Nd–Fe–B magnets by Croat *et al* at General Motors in 1984 [5] coincided with that of sintered magnets by Sagawa *et al* at Sumitomo [6]. In the melt-spinning method, a jet of molten alloy is fired at a water-cooled copper wheel, which is rotating at a high speed. The liquid solidifies at a cooling rate of up to 10^6 K s^{-1} and fine, brittle ribbons are thrown off the wheel. The melt undergoes rapid quenching and iron-free material can be produced. Depending on the wheel speed, ejection conditions and melt temperature substantial undercooling below the equilibrium freezing temperature and, consequently, a very high frequency of crystal nucleation are achieved. The analysis of the devitrification kinetics for the amorphous phase revealed a relatively low growth rate of the $Nd_2Fe_{14}B$ phase. This leads to the ultrafine grain size of typically 20–50 nm on annealing, during which coercivity is developed [47–49].

The randomly oriented grain structure results in magnetically isotropic magnets, with the remanent magnetization, B_r, and $(BH)_{max}$ limited to 0.5 and 0.25, respectively, of the values obtainable for ideal microstructures consisting of single-domain grains and with full crystallographic alignment (see equation (1)). The ribbons are usually mixed with some kind of polymer resin and are then injection or compression moulded (Magnequench, MQ1). Larger remanences can be obtained when hot pressing the crushed ribbons to full density (MQ2) followed by hot deforming (die upsetting, see section 3.5) the compact (MQ3) and finally crushing the forgings. This rather complicated route leads to an anisotropic powder which can be exposed to a magnetic field in order to obtain aligned NdFeB bonded magnets with energy products of more than 140 kJ m^{-3}.

The analogous PrFeB-based compounds can be produced by melt spinning [8, 50] and are of particular relevance for low-temperature applications as they show no spin reorientation down to 4.2 K (which occurs at 135 K for $Nd_2Fe_{14}B$) and are also of interest for hot-deformed magnets (see section 3.5).

The intrinsic magnetic properties of the related $Nd_2Fe_{14}C$ are very similar to those of the corresponding

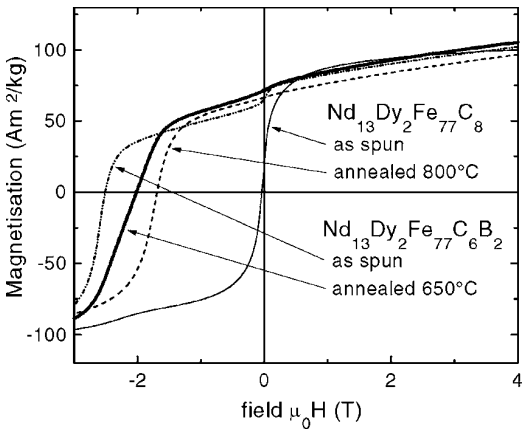

Figure 9. Demagnetization curves of melt-spun $Nd_{13}Dy_2Fe_{77}C_8$ before and after annealing at 800 °C and of $Nd_{13}Dy_2Fe_{77}C_6B_2$ before and after annealing at 650 °C (from Yang *et al* [52]). The magnetic properties of the ribbons are: coercivity $\mu_0 H_c = 1.8$ T, remanence $B_r = 0.63$ T, maximum energy product $(BH)_{max} = 70$ kJ m^{-3}, Curie temperature $T_c = 555$ K for $Nd_{13}Dy_2Fe_{77}C_8$ and $\mu_0 H_c = 2.0$ T, $B_r = 0.69$ T, $(BH)_{max} = 89$ kJ m^{-3}, $T_c = 590$ K for $Nd_{13}Dy_2Fe_{77}C_6B_2$.

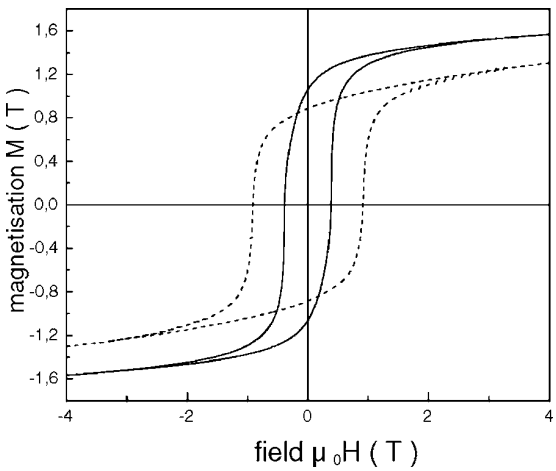

Figure 10. Hysteresis loop of mechanically alloyed, two-phase $Nd_8Fe_{88}B_4$ (full curves) after optimized annealing treatment in comparison with intensively milled, single-phase $Nd_{11.8}Fe_{82.3}B_{5.9}$ (broken curves); (from Crespo *et al* [63]).

borides: the anisotropy field is slightly higher, the Curie temperature and magnetization slightly lower (see table 1). The formation of the $R_2Fe_{14}C$ compound proceeds via a peritectoid reaction from the $R_2Fe_{17}C_2$ and RFeC phases. This solid-state transformation temperature can be increased very effectively with small boron substitutions for carbon [51] and better control of the microstructure compared to the NdFeB system is possible (so-called 'ingot-magnets'). In the as-quenched $Nd_{13}Dy_2Fe_{77}C_8$ ribbons, which consist mainly of the 2:17 and α-Fe soft magnetic phases, very low coercivities $\mu_0 H_c \leqslant 0.1$ T are observed. However, as-quenched $Nd_{13}Dy_2Fe_{77}C_6B_2$ ribbons show a coercivity as high as 2.5 T at room temperature. This is due to the fact that the as-quenched $Nd_{13}Dy_2Fe_{77}C_6B_2$ ribbons consist almost completely of the 2:14:1 phase. Figure 9 shows typical demagnetization curves of $Nd_{13}Dy_2Fe_{77}C_8$ before and after annealing at 800 °C and of $Nd_{13}Dy_2Fe_{77}C_6B_2$ ribbons before and after annealing at 650 °C for 15 min, respectively [52].

Melt-spun precipitation hardened $Sm_2(Co, Cu, Fe, Zr)_{17}$ magnets with an abnormal temperature dependence of the coercivity have also been produced recently [53] as well as magnetically anisotropic $SmCo_5$ ribbons using single-roller melt spinning at low velocity [54].

3.2.2. Mechanically alloyed magnets. Mechanical alloying, originally established for superalloys [55], circumvents many limitations of conventional alloying as it is, like rapid quenching, a non-equilibrium processing technique and thus can be used for the preparation of metastable alloys. An interdiffusional reaction, enabled by the formation of ultrafine layered composite particles during high-energy ball milling, leads to the mixing of the elements. Depending on the thermodynamics of the alloy system, the energy input during milling and the mechanical workability of the starting powders, the alloying can take place during milling or during a subsequent heat treatment. Schultz *et al* reported in 1987 [56] that in the case of Nd–Fe–B magnets, a layered microstructure of Fe and Nd is formed with B particles remaining undeformed and embedded in the interfaces. The hard magnetic $Nd_2Fe_{14}B$ phase is then formed at relatively low annealing temperatures of 600–700 °C and short reaction times of 10–30 min, which is due to the extremely fine distribution of the reactants.

In the following years, a number of R–T compounds were synthesized from the elemental powders, including Sm–Co [57], SmFeTi [58], SmCoFe [59], $Sm_2Fe_{17}N_{2.6}$ [60, 61] and $Sm_2Fe_{14}Ga_3C_2$ [62]. Typical as-milled structures consist of nanocrystallites of α-Fe and an R-rich amorphous phase [56], but also of a single amorphous phase as in the case of $SmCo_5$ [57]. All these compounds have a randomly oriented nanocrystalline structure after mechanically alloying and annealing, and with crystallite sizes of 10–50 nm.

A modification of mechanical alloying is the intensive milling technique, where an alloy is exposed to high-energy ball milling rather than the elemental powders. Hysteresis loops of mechanically alloyed, two-phase $Nd_8Fe_{88}B_4$ after an optimized annealing treatment and of intensively milled, single-phase $Nd_{11.8}Fe_{82.3}B_{5.9}$ (from [63]) are shown in figure 10. Nanostructured $PrCo_5$ powders have also been synthesized by intensive milling for 4 h and subsequent annealing for 1 min at 800 °C, resulting in a coercivity of 16.3 kOe, coercivities could be improved further by increasing the Pr content [64]. A comparison of the demagnetization curves of intensively milled (annealed at 600 °C) and HDDR (see section 3.3.1) processed $Nd_{14.6}Dy_{1.0}Fe_{75.8}B_{8.3}Zr_{0.3}$ alloy is presented in figure 11. A typical differential scanning calorimetry (DSC) curve illustrating the crystallization behaviour of the intensively milled material is shown in figure 12, the chosen annealing temperatures are usually slightly higher than the crystallization temperature. Recently, it was demonstrated large-scale intensive milling (50 kg charges) of NdFeCoGaB powders led to good magnetic properties suitable for hot pressing and hot deformation [65].

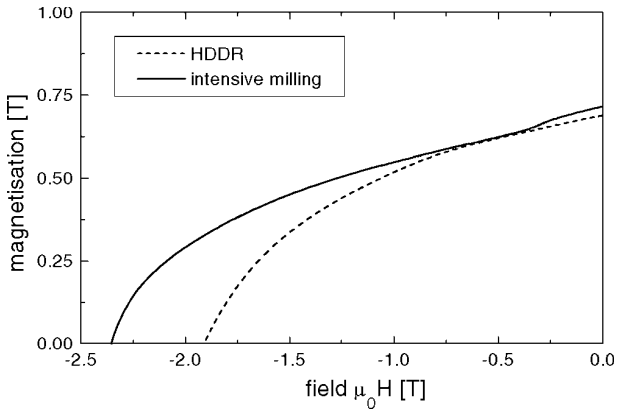

Figure 11. Comparison of demagnetization curves of intensively milled (60 h) and annealed (30 min at 600 °C) and HDDR processed (disproportionation at 820 °C for 100 min and recombination at 780 °C for 15 min) $Nd_{14.6}Dy_{1.0}Fe_{75.8}B_{8.3}Zr_{0.3}$ alloy.

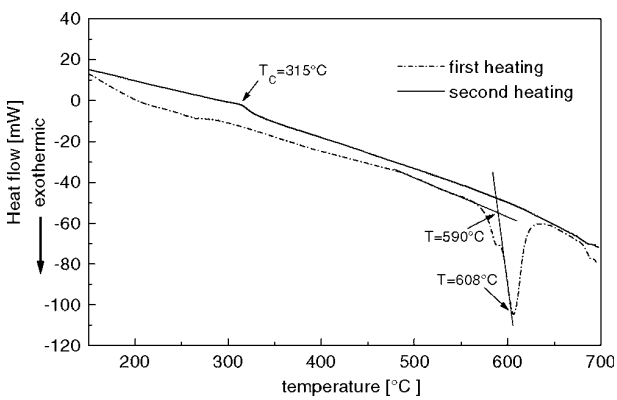

Figure 12. DSC curves of intensively milled $Nd_{14.6}Dy_{1.0}Fe_{75.8}B_{8.3}Zr_{0.3}$ alloy showing the exothermic crystallization at $T = 608\,^{\circ}C$ and its onset during first heating and on a second heating, the Curie temperature at $T_c = 315\,^{\circ}C$.

3.2.3. Remanence-enhanced magnets. A ferromagnetic exchange interaction can lead to enhanced remanences in isotropic hard magnetic materials, larger than those predicted by the Stoner–Wohlfarth theory [66] for systems of isotropically oriented, magnetically uniaxial, non-interacting single-domain particles where $M_r/M_S \leqslant 0.5$, provided the grain sizes are in the nanocrystalline range and no additional phases are found at the grain boundaries. This coupling causes the magnetization around the boundaries of the crystallites, whose easy axes are unfavourably aligned with respect to the original magnetizing field, to deviate from their respective easy axes. The interaction is driven by a quantum mechanical coupling of the electron spins, leading to a reduction in the total magnetic energy when the magnetic moments are parallel. The intrinsic properties and micromagnetic parameters, as shown in table 1, together with the actual grain sizes, which depend on the processing conditions, determine the effectiveness of the exchange coupling and thus the degree of remanence enhancement. Assemblies of hard magnetic grains are termed single-phase exchange coupled magnets (type (II) in figure 2 and broken curve figure 10), whereas assemblies of hard magnetic (to provide high coercivity) and soft magnetic (to provide high magnetization; $J_s(\alpha\text{-Fe}) = 2.16$ T) phases are called nanocomposite magnets (type (III) in figure 2 and full curve in figure 10). These high energy density magnets, usually synthesized by melt spinning or mechanical alloying and subsequent controlled nucleation or crystallization (more recently also by reactive milling and recombination (see section 3.3.2)), are of great commercial interest because no magnetic alignment and less of the costly R element are required. An effective coupling occurs when the soft regions with a small anisotropy are no larger than a few times the exchange length l_{ex}, i.e. less than 20 nm ($l_{ex} = (A/\mu_0 M_S^2)^{1/2}$, with A being the exchange stiffness in joules per metre, proportional to T_C; note: for magnetically hard regions $l_{ex} = (A/K_1)^{1/2}$ applies). However, it is important to note that the validity of equation (1) is limited by $\mu_0 H_C \geqslant J_r/2$ and hence a simple increase in the remanence by increased Fe or Co content does not automatically lead to higher energy densities.

A number of reports have been published on $Nd_2Fe_{14}B$, $Nd_2Fe_{14}B/\alpha$-Fe, $Nd_2Fe_{14}B/Fe_3B$, $Sm_2Fe_{17}N(C)_x/Fe$ and $Pr_2Fe_{14}B/\alpha$-Fe exchange coupled systems [67–77]. Coehoorn *et al* [70] reported that the crystallization of melt-spun $Nd_4Fe_{78}B_{18}$ amorphous alloy results in a nanocomposite magnet consisting of only 15 vol.% hard magnetic $Nd_2Fe_{14}B$ phase, but of 73 vol.% Fe_3B and 12 vol.% Fe soft magnetic phases with $M_r/M_S = 0.8$ and an energy product of $(BH)_{max} = 95$ kJ m^{-3}. Eckert *et al* [78] showed that it is the interaction between the soft and the hard magnetic phases which result in the specific hysteresis loop and the very steep recoil curves [79]. The theoretical description by Kneller and Hawig [19] led to the terminology 'exchange-spring magnet', basically describing that the systems remains reversible up to a large opposing field and that the magnetization of the soft phase may rotate out of its preferred direction in zero field without inducing irreversible switching of the hard magnetic grains. It was predicted that an optimum microstructure would consist of a homogeneous dispersion of a hard phase in a soft phase, both on a 5–10 nm scale. This microstructure can be synthesized by annealing a supersaturated metastable alloy, i.e. nucleation and crystallization from the glassy state. More detailed analysis showed that a metastable $Fe_{23}B_6$ precursor is essential during the crystallization sequence, because this is the only phase that is capable of dissolving the large Nd atoms, and from which the $Nd_2Fe_{14}B$, Fe and Fe_3B phases will subsequently precipitate out.

Several studies have been carried out in order to optimize the magnetic properties by microalloying. Si addition was shown to lead to refined grain sizes and hence more effective coupling in the stoichiometric compound [80]. The grain growth inhibiting effects of other additives such as Al, Ga and Co have been investigated in depth [81, 82]. More recently, Ping *et al* [83] showed that it is not only the reduction in the grain size which improves the properties, but the change in the volume fraction of the $Nd_2Fe_{14}B$ phase due to the non-uniform distribution of the additives. Sano *et al* [84] showed that in the case of a $Nd_5Fe_{74}B_{18}Cr_3$ alloy, the Cr atoms partitioning in the Fe_3B phase leads to a stabilization of the latter phase, thereby modifying the tie lines in the phase diagram. Ping *et al* [85] performed detailed studies on the crystallization kinetics of a $Nd_2Fe_{14}B/Fe_3B$ alloy

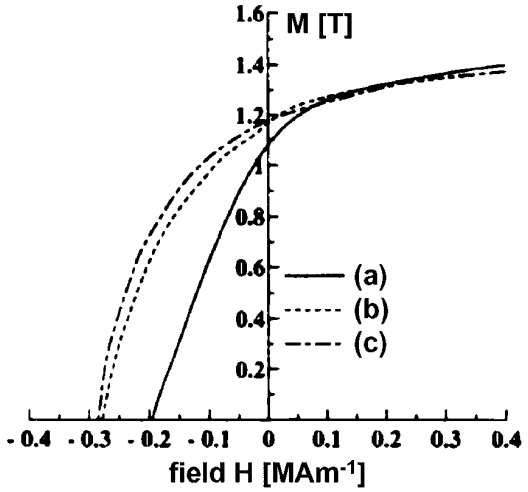

Figure 13. Demagnetization curves of (a) $Nd_{4.5}Fe_{77}B_{18.5}$, (b) $Nd_{4.5}Fe_{76.8}B_{18.5}Cu_{0.2}$ and (c) $Nd_{4.5}Fe_{75.8}B_{18.5}Cu_{0.2}Nb_1$ melt-spun ribbons annealed for 10 min at 600 °C (from Ping *et al* [85]).

microalloyed with Cu and Nb and found that a grain size reduction and improved magnetic properties (see figure 13) can be achieved. They also proposed the initial formation of Cu clusters which serve as nucleation centres for the Fe_3B primary crystals.

Partitioning of the additives will change the intrinsic properties of the various phases and hence the strength of the interaction, which, in addition, also depends on the grain sizes of both types of phases. Micromagnetic modelling has become an important tool to predict and optimize the exchange coupling between the soft and hard magnetic phases [86–93]. Numerical micromagnetics predict, for example, for systems consisting of $Nd_2Fe_{14}B$, α-Fe and Fe_3B phases and varying grain sizes and volume fractions coercivities in the range of 340–610 kA m^{-1} and remanences in the range of 1.4–1.1 T [93].

3.3. Magnets obtained by hydrogen assisted processing

3.3.1. HDDR processed magnets. Strictly, conventional HDDR [94–96] does not lead to nanoscale (usually defined as <100 nm) material, as the final product shows typical grain sizes of around 300 nm. However, the intermediate, disproportionated state is certainly nanoscale. The simplicity of the process is quite striking as it relies only on a reversible hydrogen-induced phase transformation, which is used to produce highly coercive $Nd_2Fe_{14}B$ powders, suitable for the production of both bonded and fully dense hot-pressed magnets. In the case of HDDR processed $Sm_2Fe_{17}N_3$-type magnets [97, 98], the applications are restricted to bonded magnets because of the limited thermal stability of the 2:17 nitride of approximately 600 °C [12]. However, the thermal stability can be improved when using $Sm_2Fe_{17-x}Ga_xC_y$ powders [99]. In the case of $Nd_2Fe_{14}B$, the HDDR process consists of two stages: firstly, the disproportionation into a finely divided mixture of neodymium hydride, iron and ferroboron, typically at 800 °C and 1 bar hydrogen, and, secondly, the recombination on desorption to the original $Nd_2Fe_{14}B$ phase, but now with a much refined grain size

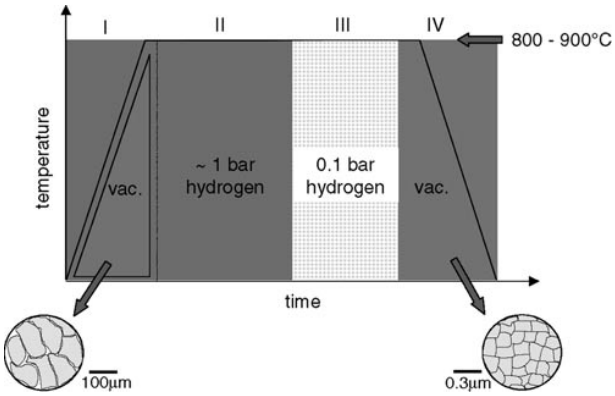

Figure 14. Schematic representation of the conventional HDDR procedure consisting of heating from room temperature to 800–900 °C in hydrogen and desorption/recombination under continuous pumping and of the modified HDDR procedure consisting of: stage I, heating under vacuum; stage II, solid disproportionation; stage III, slow recombination under a partial hydrogen pressure; and stage IV, full desorption.

(see the schematic presentation in figure 14). The HDDR reactions in the two systems can be described as

$$Nd_2Fe_{14}B+(2\pm x)H_2 \Leftrightarrow 2NdH_{2\pm x}+12Fe+Fe_2B\pm\Delta H \quad (3)$$

and

$$Sm_2Fe_{17} + (2 \pm x)H_2 \Leftrightarrow 2SmH_{2\pm x} + 17Fe \pm \Delta H'. \quad (4)$$

At lower temperatures the interstitial hydride is formed, representing a metastable state (hydrogen solid solution) and the forward reaction as described in (3) or (4), i.e. the formation of the thermodynamically more stable binary R hydride, is prevented by the absence of sufficient kinetics at room temperature. The interstitial absorption, leading to the so-called HD (hydrogen decrepitation) [31], results in a large volume expansion of about 4.8 vol.% in the $Nd_2Fe_{14}B$–H [100] and 3.4 vol.% in the Sm_2Fe_{17}–H [101]. In $Nd_{15}Fe_{77}B_8$ the HD is initiated by the differential expansion due to the formation of the neodymium hydride at the grain boundaries. The HD process is widely used in the production of sintered NdFeB-type magnets as it is an effective means of providing particulate material that is very suitable for subsequent milling. Inter- and intragranular failure leads to single crystal powder. HD can be avoided by introducing hydrogen at elevated temperatures, which results in the disproportionation without cracking, the so-called 'solid-HDDR' process [102].

Figure 15(a) shows the typical absorption reactions of a $Nd_{14.6}Dy_{1.0}Fe_{75.8}B_{8.3}Zr_{0.3}$ alloy during heating in a hydrogen atmosphere, namely the low-temperature interstitial absorption by the 2:14:1 phase (A) and the disproportionation of the same phase (C) according to equation (3). The x-ray diffraction (XRD) pattern of figure 15(b) shows the phases present after disproportionation. A demagnetization curve of the conventionally HDDR processed $Nd_{14.6}Dy_{1.0}Fe_{75.8}B_{8.3}Zr_{0.3}$ alloy is also shown in figure 11. In this case the long disproportionation time of 100 min leads to magnetically isotropic powder with a high coercivity of 1.8 T. The hydrogen absorption and desorption characteristics are affected by alloy additions. In particular, it has been found that Co and

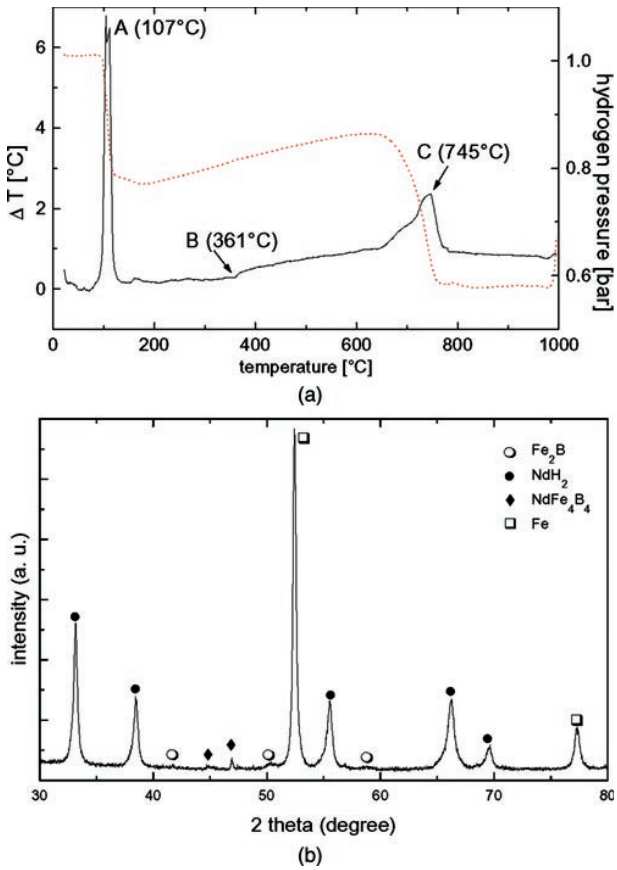

Figure 15. (a) Differential thermal analysis (solid line) and temperature pressure analysis (dotted line) on heating a $Nd_{14.6}Dy_{1.0}Fe_{75.8}B_{8.3}Zr_{0.3}$ alloy in 1 bar hydrogen showing: A, interstitial absorption; B, the Curie temperature of the 2:14:1 hydride; and C, disproportionation (this exothermic reaction here is bimodal and shifted to a relatively high temperature, which could be attributed to the addition of Zr. (b) XRD pattern of the alloy after disproportionation showing the typical reaction products (note that the $NdFe_4B_4$ phase is already present in the cast structure).

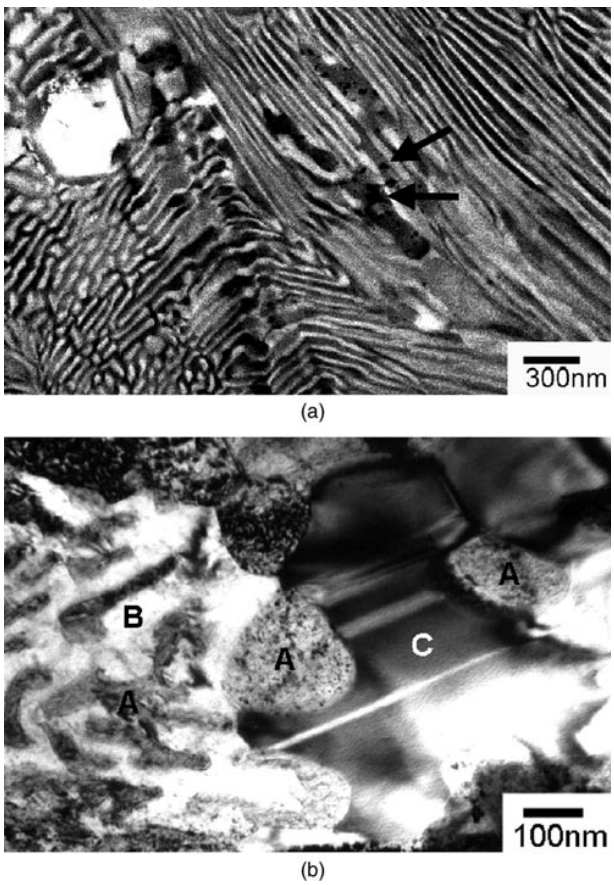

Figure 16. (a) High-resolution SEM image in the backscattered mode of a solid disproportionated NdFeB alloy showing the rod-like Nd hydride phase (white), α-Fe (dark grey) and finely dispersed, metastable Fe_3B grains (indicated by the arrows). (b) Bright field TEM image of a conventionally disproportionated NdFeB alloy showing the transformation from a rod-like to a granular structure (A denotes Nd hydride, B denotes α-Fe and C denotes Fe_2B with typical stacking faults).

Ga accelerate the recombination reaction and shift its onset to lower temperatures and Zr makes the disproportionation reaction sluggish [103–105]. An example of a disproportionated structure of a ternary NdFeB-type alloy is given in figure 16(a). The disproportionation products Nd hydride and α-Fe initially form a fine lamellar type structure, typical for solid disproportionated samples [102, 106]. In the TEM bright field image of figure 16(b) it can be seen how this structure transforms into a granular type structure, typical for conventionally processed samples or long annealing times in hydrogen [107].

Recently, it was shown that HDDR of $Sm_2Fe_{16}Ga$ [108] and Sm_2Co_{17} [109] is also successful when carried out at high hydrogen pressures. High hydrogen concentrations in both, the ternary and binary hydride, can be achieved when using these more severe hydrogenation conditions. A microstructure generated by high-pressure disproportionation, using for example a 40 bar starting pressure and lower temperatures such as 600 °C shows a further grain refinement [110] compared to a disproportionated mixture of, for example, Sm hydride and α-Fe induced by standard conditions [111]. The effect of compositional changes such as the substitution of Fe by Co in $Sm_2(Fe, Co)_{17}$ on the thermodynamic stability of such compounds is described qualitatively in figure 17(a). The Co substitution results in the situation that the tangent construction between the two disproportionation products is intersected by the new minimum in the free enthalpy of the Sm_2Co_{17} phase. The favourable effect of the high hydrogen pressures on the disproportionation shown in figure 17(b) could be explained in terms of a decrease of the free enthalpy of the samarium hydride with the increasing hydrogen pressure to the extent that the reaction is allowed to proceed.

A topic of particular interest is the inducement of a crystallographic and thus magnetic texture using the HDDR method. Nanocrystalline materials such as mechanically alloyed, intensively milled, rapidly quenched and HDDR produced powders are typically isotropic and therefore usually require a hot compaction and deformation (die-upsetting) procedure (see section 3.5) in order to generate a texture leading to the high remanences necessary for high-performance magnets [112]. However, the HDDR process offers the unique advantage of producing powder in an

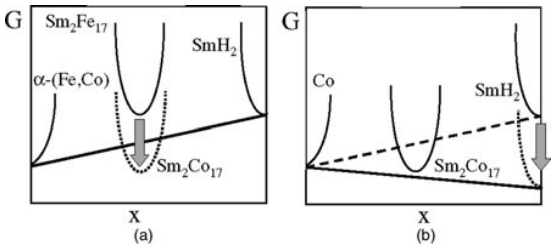

Figure 17. Schematic free enthalpy diagram of $Sm_2(Fe, Co)_{17}$ alloys (with $0 \leqslant x$ (at.% Sm) $\leqslant 1$) illustrating (a) the decrease of G by the Co substitution making the disproportionation of Sm_2Co_{17} under the standard conditions impossible and (b) the increased hydrogen pressure decreases the free enthalpy of the Sm hydride and therefore the disproportionation can take place.

anisotropic form ('MQA-T'), provided the right processing conditions and compositions are chosen [113], without having to go through the rather expensive route applied for the MQ3 material (see section 3.2.1). The magnetic properties of the pre-aligned (in a transverse field of ∼2 T) and hot-pressed derivative of this MQA-T material were determined to be $\mu_0 J H_c = 1.2$ T and $B_r = 1.2$ T and the degree of alignment is illustrated in the Kerr micrograph of figure 18 [114]. Here the preferred direction of magnetization is perpendicular to the imaging plane, and a maze-like pattern of interaction domains is observed, consistent with magnetically-interacting grains with well aligned c-axes and grain sizes not exceeding the critical single-domain diameter. The average width of the interaction domains is large (∼2 μm) for the MQA-T material which can be attributed to a local high degree of order. A 'memory-cell' model [115] has been proposed to explain the inducement of magnetic anisotropy and has been supported by thermodynamic arguments [116] and electron microscopy studies [117]: nanoscale $Nd_2Fe_{14}B$-type particles rich in additives such as Co, Ga or Zr remain unaffected by the disproportionation reaction and therefore retain the orientation of the original grains. Recently, an Fe_3B phase has been detected within the structure of a solid-disproportionated Co and Ga containing alloy exhibiting a 'one-to-one' crystallographic relationship with the original $Nd_2Fe_{14}B$ phase and this phase could act as an anisotropy mediating phase [118]. On the other hand, it has been shown that it is possible to induce anisotropic features in a ternary alloy [119, 120] by applying a modified HDDR procedure as shown in figure 14. This procedure includes a solid-disproportionation step and a slow recombination under a partial hydrogen pressure [121]. The latter step facilitates the control of the grain growth during the strongly endothermic desorption stage. However, there appears to be a particular difficulty when increasing the remanence, i.e. the degree of texture, while maintaining a reasonable coercivity. These observations of the ternary compound shed new light on the above 'memory-cell' model for the inducement of magnetic anisotropy as the coexistence of the disproportionated constituents and residual, nanoscale $Nd_2(Fe, Co, Ga)_{14}B$ no longer appears to be a feasible explanation for the phenomena observed. The key could lie in the type of disproportionated structure generated by the different procedures. Conventional processing leads to a granular structure whereas solid disproportionation results in a rod-like or lamellae-like structure (see figure 16(a)) in which an

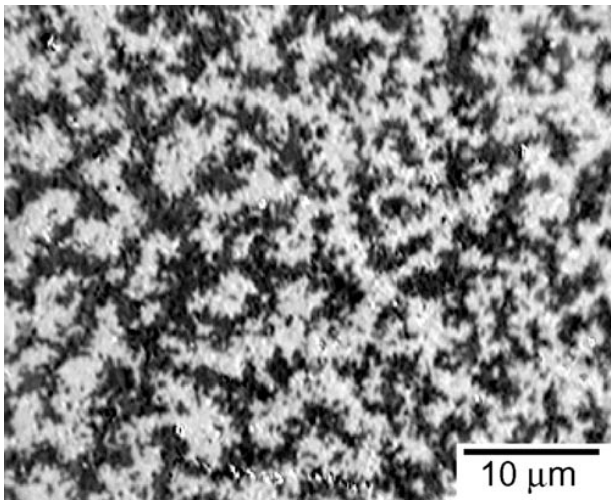

Figure 18. High-resolution Kerr micrograph of hot-pressed anisotropic HDDR powder (MQA-T: $\mu_0 J H_c = 1.2$ T and $B_r = 1.2$ T) material with the preferred direction of magnetization perpendicular to the imaging plane. Magnetically-interacting grains with well aligned c-axes and grain sizes not exceeding the critical single-domain diameter result in a maze-like pattern of interaction domains.

intermediate tetragonal Fe_3B phase is embedded [107]. The driving force for the strongly endothermic recombination reaction under a partial hydrogen pressure will be reduced compared to that of a vacuum recombination. This in turn will affect the nucleation and growth of the $Nd_2Fe_{14}B$ phase, which should be preferential rather than random in the former case and therefore not only enhance the anisotropic features but also impede excessive grain growth.

The existence of residual, nano-scale grains stabilized by additives should also be possible for Sm_2Fe_{17}-type alloys as similar disproportionation retarding and recombination accelerating effects have been observed [104, 108]. However, the absence of iron boride phases in the Sm–Fe system and thus of an anisotropy mediating phase is the striking difference between the two systems, and therefore a texture after the HDDR process is unlikely to be expected for the Sm_2Fe_{17}-type material.

3.3.2. Reactive milling in hydrogen. Mechanically-induced gas–solid reactions under non-equilibrium conditions can also be used to hydrogen disproportionate compounds which are thermodynamically much more stable than those based on $Nd_2Fe_{14}B$ and Sm_2Fe_{17} [122, 123]. This reactive milling procedure consists of ball milling in enhanced hydrogen pressures and temperatures; this is followed by vacuum annealing to ensure the full desorption and recombination.

The effect of reactive milling on Sm_2Co_{17} alloys is illustrated in the XRD patterns of figure 19; after milling, the reflections of $SmH_{2+\delta}$ and fcc Co can be seen. The extremely broad reflections are caused by a very fine nanocrystalline structure of these phases: the average grain size of the $SmH_{2+\delta}$ phases was estimated to be around 9 ± 2 nm using the Williamson–Hall method [124]. This is a much finer structure than that of the disproportionated Sm_2Fe_{17}-type or $Nd_2Fe_{14}B$-type materials prepared by the

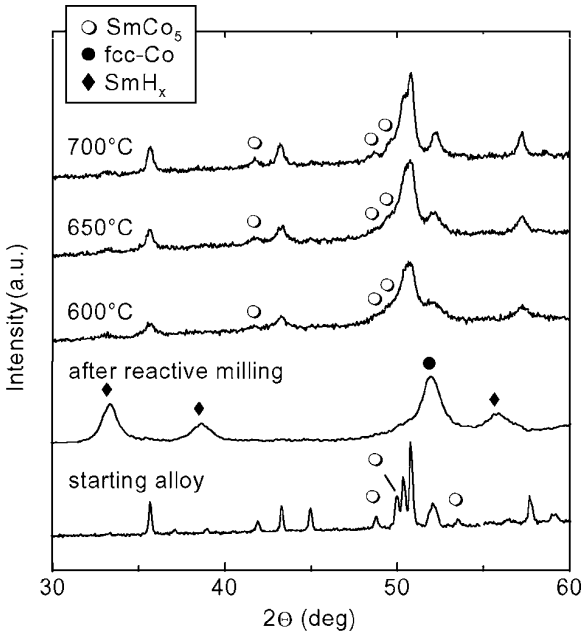

Figure 19. XRD patterns of the starting Sm_2Co_{17} alloy (with excess Sm), the reactively milled material (the broad reflections indicate very fine grain sizes in the disproportionated state) and powders recombined at various temperatures.

conventional HDDR method [106, 111]. Figure 19 also shows the XRD patterns of the Sm_2Co_{17}-type powders for different recombination temperatures. 1:5-type phase reflections due to excess Sm in the initial alloy can be seen in addition to the reflections of the 2:17-type phase. A decreasing mean peak width can be observed with increasing recombination temperatures due to the larger average grain sizes. Grain sizes of 18 ± 6 nm (600 °C), 25 ± 8 nm (650 °C) and 29 ± 4 nm (700 °C) were estimated from the XRD patterns for the recombined samples [123]. It was observed that, despite the presence of two different phases, the demagnetization curves of the Sm_2Co_{17}-type powders have a magnetically single-phase-like appearance for the low recombination temperatures. The remanence $J_r = 0.71$ T for the sample recombined at 600 °C is significantly higher than the theoretical maximum value $J_s/2 = 0.65$ T [21] of isotropically distributed single-domain Sm_2Co_{17} particles; which is attributed to the effect of exchange coupling between the nanoscaled grains. It must also be taken into account that the amount of the $SmCo_5$ phase within the sample should decrease the J_r value even further due to the lower value of the saturation magnetization compared to that of Sm_2Co_{17} (see table 1).

Recently, it was also demonstrated that reactive milling can be applied successfully to disproportionate the entire $Nd_2(Fe, Co)_{14}B$ series and the effect of remanence enhancement was more pronounced in the $Nd_2Co_{14}B$ alloy due to smaller grain sizes in this alloy [125].

In summary, gas–solid reactions of R–T compounds (R_nT_m) with hydrogen are an alternative route to mechanical alloying, intensive milling or rapid quenching for the preparation of amorphous or nanocrystalline materials. Depending on thermodynamics (stabilities of the starting alloy and reaction products) and kinetics (temperature, hydrogen pressure and possibly mechanical activation) an interstitial modification resulting in a ternary hydride (c-$R_nT_mH_x$), an amorphous hydride (a-$R_nT_mH_x$)—the so-called hydrogen-induced amorphization [126] or a disproportionation into a binary R hydride and the T ($nRH_x + mT$) can occur (see figure 20). Metastable phases will be the reaction products when the activation, either thermally or mechanically, is insufficient to form the necessary concentration gradient of metal atoms and only hydrogen diffusion is possible ('chemical frustration' [126]). Hydrogen-induced amorphization was recently demonstrated for a $SmFe_3$ alloy using enhanced hydrogen pressures [127].

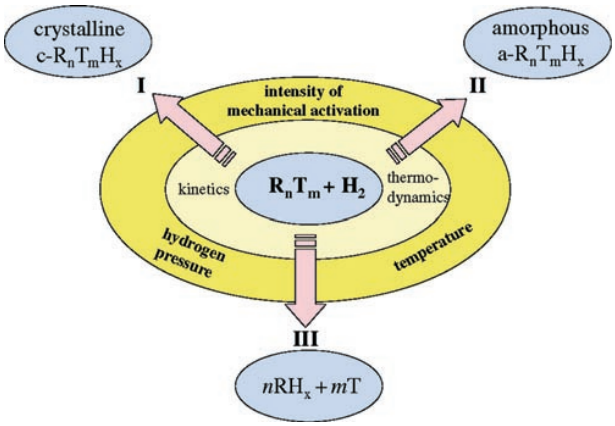

Figure 20. Schematic representation of hydrogen gas–solid reactions of R–T compounds. Depending on thermodynamics and kinetics a ternary hydride (I, c-$R_nT_mH_x$), an amorphous hydride (II, a-$R_nT_mH_x$) or a binary R hydride and the T (III, $nRH_x + mT$) is formed.

3.4. Interstitially modified R_2Fe_{17} magnets

Interstitial nitrogen or carbon in rhombohedral R_2Fe_{17} (Th_2Zn_{17} structure) compounds changes the intrinsic magnetic properties dramatically, because not only is the Curie temperature increased due to the lattice expansion (in the case of nitrogen in Sm_2Fe_{17} a 6 vol.% expansion and an increase in T_C from 116 to 476 °C are observed), but also the crystalline electric field is modified by the nitrogen or carbon atoms, which occupy the large interstial 9e sites, leading to a change of the magnetocrystalline anisotropy from easy plane to easy axis [128]. The corresponding $R_2Fe_{17}Z_x$ ($0 \leqslant x \leqslant 3$) nitrides and carbides are, in contrast to the binary R_2Fe_{17} compounds, promising candidates for permanent magnetic materials. Ternary carbides $R_2Fe_{17}C_x$ ($x \leqslant 1.5$) can be prepared by standard casting techniques, higher C concentrations can be achieved by either substituting Ga for part of the Fe in the cast materials or by exposing fine particles of the binary compound to hydrocarbon gases at elevated temperatures (see reviews by Skomski *et al* [129] or Fuji and Sun [130]). Similarly, a simple gas phase nitrogenation according to (5) can be carried out at 1 bar nitrogen gas and temperatures of about 400–500 °C.

$$2R_2Fe_{17} + 3N_2 \Rightarrow 2R_2Fe_{17}N_3. \qquad (5)$$

The absorption of nitrogen atoms takes place once the temperature is high enough to overcome the activation

energy for the absorption process. This gas–solid reaction consists of adsorption of the gas molecules, their dissociation and subsequent chemisorption of, for example, N atoms and finally long-range diffusion into the metal matrix. A detailed understanding of this irreversible nitrogenation process is necessary in order to optimize the final magnetic properties, and it is still a matter of discussion whether, in a thermodynamic equilibrium, a solid solution of ternary nitrides with fully nitrided and non-nitrided layers are obtained. The relatively slow diffusion of the N atoms into the matrix makes it necessary to use fine ground particles obtained after intensive milling [131] or HDDR [132]; microcracks and microcrystals provide fast diffusion paths so that shorter annealing times and lower temperatures can be used. However, the latter remain critical processing parameters as a decomposition in RN and Fe according to equation (6) is the preferred reaction from a thermodynamical point of view:

$$R_2Fe_{17} + N_2 \Rightarrow 2RN + 17Fe \qquad (6)$$

Long-range diffusion of metal atoms is required for this reaction and insufficient kinetics make the preparation of ternary nitrides possible despite the metastability of the latter compared to the binary nitride and the Fe metal. The limited thermal stability of the ternary nitrides restricts the applicability of this class of compounds to metal or polymer-bonded magnets. The decomposition temperature can be increased by additions, such as Al, Si or Ga [133–135], and in general it can be stated that the carbides are superior to the nitrides in terms of their thermal stability. Very small grain sizes are needed for highly coercive powders and the appropriate processing routes have been reviewed by Müller *et al* [136].

Figure 21 gives a comparison of demagnetization curves of $Sm_2Fe_{17}N_3$ prepared by mechanical alloying the binary compound and subsequent nitrogenation of the powder annealed at 750 °C and $Sm_2Fe_{15}Ga_2C_2$ prepared by mechanical alloying the melt-carburized compound followed by annealing at 800 °C [137]. Higher saturation magnetization and anisotropy field lead to higher remanence and coercivity in the case of the former alloy; however the thermal stability of the latter alloy is much improved and opens up the hot-pressing processing route in order to obtain fully dense magnets.

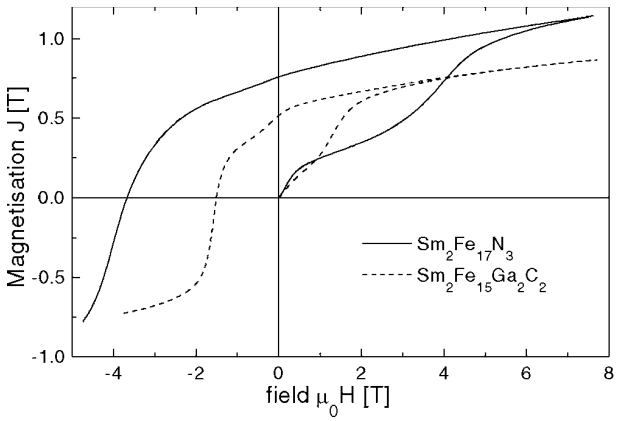

Figure 21. Comparison of demagnetization curves of $Sm_2Fe_{17}N_3$ prepared by mechanical alloying the binary compound and subsequent nitrogenation and annealing (750 °C) and $Sm_2Fe_{15}Ga_2C_2$ prepared by mechanical alloying the melt-carburized compound followed by annealing at 800 °C.

3.5. Textured magnets by hot deformation

In addition to the powder metallurgical sintering route, where an external magnetic field is used to align microcrystalline single-crystal particles, and the anisotropic HDDR route, where a field is used to align particles consisting of many 300 nm sized grains with a preferred orientation, the hot-deformation-induced texturing of cast alloys or fine grained materials provides a third option for producing anisotropic RPMs with maximized energy densities. A grain alignment along the *c*-axis of the tetragonal 2:14:1 phase based on either Nd–Fe–B or Pr–Fe–B alloys perpendicular to the plastic flow is achieved after high-temperature compressive deformation.

The hot extrusion of encapsulated Nd–Fe–B [138], the hot rolling of Pr–Fe–B–Cu with high strain rates (1–10 s^{-1}) enabling the processing of large amounts of material [139] and the hot pressing of Pr–Fe–B at 1000 °C [140], are examples of the hot working of cast materials as an 'in principle' very economic means of producing anisotropic, fully dense magnets. The main advantage of hot working cast materials is the omission of handling fine powdered materials with all the attendant contamination problems. The disadvantages are less orientation control and more limited shapes.

The hot deformation of fine grained materials involves, in the first instance, the production of a fully dense isotropic precursor at about 725 °C, which is followed by placing this compact in an oversized die cavity, where the die upsetting is carried out at similar temperatures. After the second step, an anisotropic magnet is obtained with the alignment of the crystallographic *c*-axes parallel to the pressing direction. Alternatively, backward extrusion [141–143] can be carried out as a second step to produce near net-shaped ring magnets which can show, especially for smaller dimensions, superior magnetic properties to sintered magnets. A radial preferential orientation is obtained, again with the *c*-axis alignment perpendicular to the material flow. Small variations in the magnetic properties have been observed along the cross section and along the axial direction of the ring magnets, which was attributed to inhomogeneities in the material flow inherent to the deformation process [144].

The key for the hot workability is the presence of a R-rich grain boundary phase which is liquid at the deformation temperature. It is proposed that preferential grain growth under stress leading to the formation of platelet shaped grains [145, 146] is responsible for the texture. This could be due to the anisotropy of crystal growth of the tetragonal $Nd_2Fe_{14}B$ phase [147] or the anisotropy of its elastic properties [148]. It has also been argued that mass transport through the Nd-rich liquid phase is the principal mechanism for the transport of matter, especially as there is no evidence of dislocations or slip lines [149]. The solution–precipitation creep model has been applied in order to elucidate the hot-deformation processes [150]. The model is based on the assumption that the above transport of matter depends on the local stress state

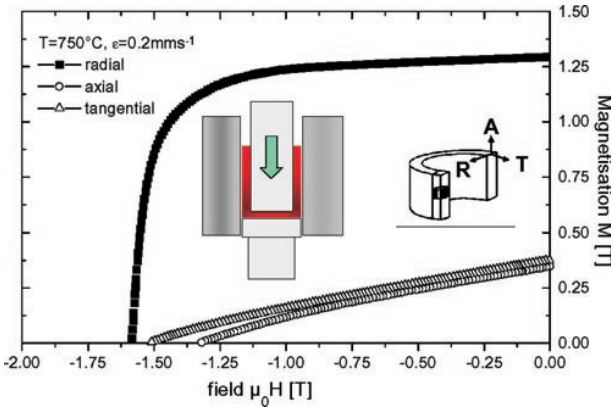

Figure 22. Demagnetization curves along the radial, axial and tangential directions of the ring magnet made from melt-spun $Nd_{13.6}Fe_{73.6}Co_{6.6}Ga_{0.6}B_{5.6}$ (MQU-F). The insert show schematic diagrams of the hot deformation process by backward extrusion and a section of the resulting ring magnet.

and thus the anisotropy of the elastic properties will play a role in the solution equilibrium between solid and liquid, that means influencing the transport of matter in this interface-controlled process.

It was shown that the hot workability, i.e. the required stress for a given strain, depends sensitively on the alloy composition and the initial grain size. It was shown that the HDDR powder requires higher deformation stresses than the melt-spun or intensively milled types [112] and that small additions of, for example, Ga can improve the hot workability remarkably, possibly due to a modified melting point and viscosity of the intergranular phase [151]. Figure 22 shows the demagnetization curves along the radial, axial and tangential directions of a backward extruded ring magnet made from melt-spun $Nd_{13.6}Fe_{73.6}Co_{6.6}Ga_{0.6}B_{5.6}$ (MQU-F) illustrating the high degree of texture and overall excellent magnetic properties [151].

4. Summary and outlook

At the time of writing, about 95% of the limit for the energy density $(BH)_{max}$ (based on the $Nd_2Fe_{14}B$ phase) can be achieved in industrially produced sintered Nd–Fe–B grades and, thus, the energy densities are close to saturation. This type of material will dominate the market more and more and will penetrate into further application areas, where currently ferrite and alnicos are still being used, as there is a general need for miniaturized and less energy consuming devices. Furthermore, completely new designs such as linear motors are possible. Future developments in the existing materials will focus on the optimization via improved processing techniques of the coercivity, H_C, as these values rarely exceed 20–30% of the anisotropy field, H_A. This will allow the use of RPMs in applications where elevated temperatures occur. Isotropic exchange-coupled magnets are on the brink of being commercialized, and anisotropic nanocomposite magnets, by an alignment of the *c*-axis of the hard nanocrystals, could be the next generation of RPMs. With regard to the processing techniques, novel methods such as mechanically induced gas–solid reactions suitable for the tuning of one- or multi-phase nanostructures for exchange-coupled magnets might be of interest and their full potential is yet to be explored.

With respect to the materials themselves, it can be stated that the binary and ternary R–T equilibrium systems have been studied extensively. However, a vast number of ternary, quaternary, etc equilibrium and non-equilibrium phases are left to be investigated. An increased importance of the modelling of the magnetization processes based on realistic micro- and nanostructures as well as the computing of magnetic ordering temperatures, structure types and equilibrium phase diagrams of multicomponent, possibly including metastable phases, systems can be expected.

Presently, there appears to be little prospect of discovering a new R–T compound with outstanding magnetic properties which could emulate NdFeB. However, this statement could be made redundant at the time of writing. The focus will be on processing the existing materials more effectively and economically and developing new designs of applications where the magnetic function is combined with, for example, electrical and mechanical functions.

Acknowledgments

Thanks are due to my colleagues at the IFW Dresden for stimulating discussions, for their cooperation and for expert assistance in many experiments; in particular, I am grateful to L Schultz, K H Müller, M Kubis, A Bollero, B Gebel, A Kirchner, A Handstein, D Hinz, D Eckert, M Wolf, R Schäfer and Y Yang. The support of part of this work by the Deutsche Forschungsgemeinschaft (SFB 463) is also acknowledged.

References

[1] Strnat K, Hoffer G, Olson J, Ostertag W and Becker J J 1967 *J. Appl. Phys.* **38** 1001
[2] Adler E and Hamann P 1985 *Proc. 4th Int. Symp. Magn. Anisotropy and Coercivity in RE-TM Alloys (Dayton, USA)* p 747
[3] Durst K D and Kronmüller H 1985 *Proc. 4th Int. Symp. Magn. Anisotropy and Coercivity in RE-TM Alloys (Dayton, USA)* p 725
[4] Brown W F 1945 *Rev. Mod. Phys.* **17** 15
[5] Croat J J, Herbst J F, Lee R W and Pinkerton F E 1984 *J. Appl. Phys.* **55** 2078
[6] Sagawa M, Fujimori S, Togawa M and Matsuura Y 1984 *J. Appl. Phys.* **55** 2083
[7] Hirosawa S, Matsuura Y, Yamamoto H, Fujimura S, Sagawa M and Yamauchi H 1986 *J. Appl. Phys.* **59** 873
[8] Goll D, Seeger M and Kronmüller H 1998 *J. Magn. Magn. Mater.* **185** 49
[9] Buschow K H J, de Mooij D B and Denissen C J M 1988 *J. Less-Common Met.* **141** L15
[10] Lui W, Zhang Z, Sun X K, Chuang Y C, Yang F and de Boer F R 1990 *Solid State Commun.* **76** 1375
[11] Strnat K J 1988 *Ferromagnetic Materials* vol 4, ed E P Wohlfarth and K H J Buschow (Amsterdam: North-Holland) p 131
[12] Coey J M D 1992 *Proc. of the 6th Int. Conf. on Ferrites (ICF6) (Kyoto, Japan 1992)* p 1064
[13] Hu Z, Yelon W B, Kaogirou O and Psycharis V 1996 *J. Appl. Phys.* **80** 2955
[14] Cadogan J M, Li H S, Margarian A, Dunlop J B, Ryan D H, Collocott S J and Davis R L 1994 *J. Appl. Phys.* **76** 1971

[15] Sakurada S, Tsutai A, Hirai T, Yanagida Y, Sahashi M, Abe S and Kaneko T 1996 *J. Appl. Phys.* **79** 4611
[16] Buschow K H J 1991 *J. Magn. Magn. Mater.* **100** 79
[17] Wang Y Z, Hadjipanayis G C, Kim A, Sellmyer D J and Yelon W B 1992 *J. Magn. Magn. Mater.* **104–107** 1132
[18] Li H S and Coey J M D 1991 *Ferromagnetic Materials* vol 6, ed K H J Buschow (Amsterdam: North-Holland) ch 1
[19] Kneller E F and Hawig R 1991 *IEEE Trans. Magn.* **27** 3588
[20] Coene W, Hakkens F, Coehoorn R, de Mooij B D, de Waard C, Fidler J and Grössinger R 1991 *J. Magn. Magn. Mater.* **96** 189
[21] Coey J M D (ed) 1996 *Rare Earth Iron Permanent Magnets* (Oxford: Clarendon)
[22] Buschow K H J 1988 *Ferromagnetic Materials* vol 4, ed E P Wohlfarth and K H J Buschow (Amsterdam: North-Holland) ch 1, p 1
[23] Buschow K H J 1997 *Handbook of Magnetic Materials* vol 10, ed K H J Buschow (Amsterdam: Elsevier, North-Holland) ch 4
[24] Fidler J, Sasaki S and Estevez-Rams E 1999 *Material Research Society Symp. Proc. Advanced Hard and Soft Magnets 1999* vol 577, p 291
[25] Endoh M and Shindo M 1994 *Proc. 13th Int. Workshop. on RE Magnets and their Applications (Birmingham, UK, 1994)* vol 1, p 397
[26] Rodewald W, Wall B and Fernengel W 1997 *IEEE Trans. Magn.* **33** 3841
[27] Fidler J and Schrefl T 1996 *J. Appl. Phys.* **79** 5029
[28] Knoch K G, Reinsch R and Petzow G 1994 *Proc. 13th Int. Workshop. on Rare Earth Magnets and their Applications (Birmingham, UK, 1994)* p 503
[29] Schneider G, Henig E T, Petzow G and Stadelmaier H H 1986 *Z. Metallkde.* **77** 755
[30] Sagawa M, Nagata H, Itatani O and Watanabe T 1995 *Proc. 2nd Int. Workshop Material Science IWOMS (Hanoi, Vietnam, October 1995)* p 635
[31] Harris I R, Noble C and Bailey T 1985 *J. Less-Common Met.* **106** L1
[32] Bernardi J, Fidler J, Sagawa M and Hirose Y 1998 *J. Appl. Phys.* **83** 6396
[33] Kaneko Y and Ishigaki N 1994 *J. Mater. Eng. Perform.* **3** 228
[34] Sagawa M and Nagata H 1993 *IEEE Trans. Magn.* **29** 2747
[35] Kim A and Camp F E 1996 *J. Appl. Phys.* **79** 5035
[36] Grieb B 1997 *IEEE Trans. Magn.* **33** 3904
[37] Rodewald W, Katter M, Wall B, Blank R, Reppel G W and Zilg H D 2000, presented at *Intermag 2000*, *IEEE Trans. Magn.* to be published
[38] Velicescu M and Schrey P 1998 *Proc. 15th Int. Workshop on RE Magnets and their Applications (Dresden, Germany, 1998)* p 411
[39] Kumar K 1988 *J. Appl. Phys.* **63** R13
[40] Ray A E and Liu S 1992 *Proc. 12th Int. Workshop on RE Magnets and their Applications (Canberra, Australia, 1992)* p 552
[41] Yang W, Ping W, Zhenhua S and Shouzeng Z 1992 *Proc. 12th Int. Workshop on RE Magnets and their Applications (Canberra, Australia, 1992)* p 249
[42] Cataldo L, Lefevre A, Ducret F, Cohen-Adat M Th, Allibert C H and Valignat N 1996 *J. Alloys Comp.* **241** 216
[43] Liu J F, Zhang Y, Dimitrov D and Hadjipanayis G C 1999 *J. Appl. Phys.* **85** 2800
[44] Liu J F, Chui T, Dimitrov D and Hadjipanayis G C 1998 *Appl. Phys. Lett.* **73** 3007
[45] Chen C, Walmer M S, Walmer M H, Liu S, Kuhl G E and Simon G K 1999 *Material Research Society Symp. Proc. Advanced Hard and Soft Magnets 1999* vol 577, p 277
[46] Lectard E, Allibert C H and Ballou R 1994 *J. Appl. Phys.* **75** 6277
[47] Hadjipanayis G C and Gong W 1988 *J. Appl. Phys.* **64** 5589
[48] Manaf A, Buckley R A, Davies H A and Leonowicz M 1991 *J. Magn. Magn. Mater.* **101** 360
[49] Croat J J 1994 *Proc. 13th Int. Workshop on RE Magnets and their Application (Birmingham, UK, 1994)* p 65
[50] Davies H A, Harland C L, Betancourt J I and Menoza G 1999 *Material Research Society Symp. Proc. 'Advanced Hard and Soft Magnets' 1999* vol 577, p 27
[51] Eisses J, de Mooij D B, Buschow K H J and Martinek G 1991 *J. Less-Common Met.* **171** 17
[52] Yang Y, Gutfleisch O, Handstein A, Eckert D and Müller K H 2000 *Appl. Phys. Lett.* **76** 3627
[53] Goll D, Kleinschroth I, Sigle W and Kronmüller H 2000 *Appl. Phys. Lett.* **76** 1054
[54] Yan A-ru, Zhang W Y, Zhang H W and Shen B 2000 *J. Magn. Magn. Mater.* **210** L10
[55] Benjamin J S 1970 *Met. Trans.* **1** 29
[56] Schultz L, Wecker J and Hellstern E 1987 *J. Appl. Phys.* **61** 3583
[57] Wecker J, Katter M and Schultz L 1991 *J. Appl. Phys.* **69** 6058
[58] Schultz L, Schnitzke K, Wecker J, Katter M and Kuhrt C 1991 *J. Appl. Phys.* **70** 6339
[59] Ding J, McCormick P G and Street R 1994 *J. Magn. Magn. Mater.* **135** 200
[60] Ding J, McCormick P G and Street R 1993 *J. Magn. Magn. Mater.* **124** 1
[61] Schnitzke K, Schultz L, Wecker J and Katter M 1990 *Appl. Phys. Lett.* **57** 2853
[62] Ding J, Shen B, McCormick P G, Street R and Wang F 1994 *J. Alloys Comp.* **209** 221
[63] Crespo P, Neu V and Schultz L 1997 *J. Phys. D: Appl. Phys.* **30** 2298
[64] Chen Z, Meng-Burany X and Hadjipanayis G C 1999 *Appl. Phys. Lett.* **75** 3165
[65] Gutfleisch O, Rodewald W, Hinz D, Grünberger W, Müller K H and Schultz L to be published
[66] Stoner E C and Wohlfarth E P 1948 *Phil. Trans. R. Soc.* A **240** 599
[67] McCallum R W, Kadin A M, Clemente G B and Keem J E 1987 *J. Appl. Phys.* **61** 3577
[68] Buschow K H J 1987 *J. Less-Common Met.* **134** L17
[69] Hadjipanayis G C and Gong W 1988 *J. Appl. Phys.* B **4** 5559
[70] Coehoorn R, Mooji D B, Duchateau J P and Buschow K H J 1988 *J. Physique* **49** C8 669
[71] Coehoorn R, Mooji D B and DeWaard C 1989 *J. Magn. Magn. Mater.* **80** 101
[72] Schultz L and Wecker J 1988 *J. Appl. Phys.* **64** 5711
[73] Hirosawa S, Kanekiyo H and Uehara M 1993 *J. Appl. Phys.* **73** 6488
[74] Manaf A, Zhang P Z, Ahamad I, Davies H A and Buckley R A 1993 *IEEE Trans. Magn.* **29** 2866
[75] Feutrill E H, McCormick P G and Street R 1996 *J. Phys. D: Appl. Phys.* **29** 2320
[76] Chen Z, Zhang Y, Hadjipanayis G C, Chen Q and Ma B 1999 *J. Magn. Magn. Mater.* **206** 8
[77] Müller K H, Eckert D, Handstein A, Wolf M, Wirth S and Martinez L L M 1994 *Proc. 8th Int. Symp. on Magnetic Anisotropy and Coercivity in Rare Earth–Transition Metal Alloys (Birmingham, UK, 1994)* p 179
[78] Eckert D, Müller K H, Handstein A, Schneider J, Grössinger R and Krewenka R 1990 *IEEE Trans. Magn.* **26** 1834
[79] Schneider J, Eckert D, Müller K H, Handstein A, Mühlbach H, Sassik H and Kirchmayr H R 1990 *Mater. Lett.* **9** 201
[80] Clemente G B, Keem K E and Bradley J P 1988 *J. Appl. Phys.* **64** 5299
[81] Neu V, Klement U, Schäfer R, Eckert J and Schultz L 1996 *Mater. Lett.* **26** 167
[82] Davies H A 1996 *J. Magn. Magn. Mater.* **157/158** 11

[83] Ping D H, Hono K, Kanekiyo H and Hirosawa S 1998 *J. Appl. Phys.* **83** 7769
[84] Sano N, Tomida T, Hirosawa S, Uehara M and Kanekiyo H 1998 *Mater. Sci. Eng.* A **250** 146
[85] Ping D H, Hono K, Kanekiyo H and Hirosawa S 1999 *Acta Metall.* **47** 4641
[86] Fukunaga H and Innoue H 1992 *Japan. J. Appl. Phys.* **31** 1347
[87] Skomski S and Coey J M D 1993 *Phys. Rev.* B **48** 15 812
[88] Rave W and Ramstöck K 1997 *J. Magn. Magn. Mater.* **171** 69
[89] Fischer R and Kronmüller H 1998 *J. Appl. Phys.* **83** 3271
[90] Fischer R and Kronmüller H 1999 *J. Magn. Magn. Mater.* **191** 225
[91] Schrefl T, Fidler J and Kronmüller H 1994 *Phys. Rev.* B **49** 6100
[92] Schrefl T, Roitner H and Fidler J 1997 *J. Appl. Phys.* **81** 5567
[93] Schrefl T 1999 *J. Magn. Magn. Mater.* **207** 45
[94] Takeshita T and Nakayama R 1989 *Proc. 10th Int. Workshop on Rare Earth Magnets and their Applications (Kyoto, Japan, 1987)* p 551
[95] McGuiness P J, Zhang X J, Yin X J and Harris I R 1990 *J. Less-Common Met.* **158** 379
[96] Gutfleisch O and Harris I R 1996 *J. Phys. D: Appl. Phys.* **29** 2255
[97] Nakamura H, Sugimoto S, Okada M and Homma M 1992 *Mater. Chem. Phys.* **32** 280
[98] Christodoulou C N and Takeshita T 1993 *J. Alloys Comp.* **196** 155
[99] Cao L, Müller K H, Handstein A, Grünberger W, Neu V and Schultz L 1996 *J. Phys. D: Appl. Phys.* **29** 271
[100] Oesterreicher K and Oesterreicher H 1984 *Phys. Status Solidi* a **85** K61
[101] Christodoulou C N and Takeshita T 1993 *J. Alloys Comp.* **194** 113
[102] Gutfleisch O, Martinez N, Verdier M and Harris I R 1994 *J. Alloys Comp.* **215** 227
[103] Fujita A and Harris I R 1994 *IEEE Trans. Magn.* **30** 860
[104] Nakamura H, Sugimoto S, Tanaka T, Okada M and Homma M 1995 *J. Alloys Comp.* **222** 136
[105] Sugimoto S, Gutfleisch O and Harris I R 1997 *J. Alloys Comp.* **260** 284
[106] Gutfleisch O, Matzinger M, Fidler J and Harris I R 1995 *J. Magn. Magn. Mater.* **147** 320
[107] Gutfleisch O, Gebel B and Mattern N 2000 *J. Magn. Magn. Mater.* **210** 5
[108] Kubis M, Gutfleisch O, Müller K H, Harris I R and Schultz L 1998 *J. Appl. Phys.* **83** 6905
[109] Handstein A, Kubis M, Gutfleisch O, Gebel B and Müller K H 1999 *J. Magn. Magn. Mater.* **192** 73
[110] Gutfleisch O, Kubis M, Handstein A, Müller K H and Schultz L 1999 *Materials Research Society Symp. Proc.* 'Advanced hard and soft magnets' vol 577, p 3
[111] Okada M, Saito K, Nakamura H, Sugimoto S and Homma M 1995 *J. Alloys Comp.* **231** 60
[112] Kirchner A, Grünberger W, Gutfleisch O, Neu V, Müller K H and Schultz L 1998 *J. Phys. D: Appl. Phys.* **31** 1660
[113] Takeshita T and Nakayama R 1992 *12th Int. Workshop on Rare Earth Magnets and their Applications (Canberra, Australia, 1992)* p 670
[114] Gutfleisch O, Eckert D, Schäfer R, Panchanathan V and Müller K H 2000 *J. Appl. Phys.* **87** 6119
[115] Harris I R 1992 *Proc. 12th Int. Workshop on Rare Earth Magnets and their Applications (Canberra, Australia, 1992)* p 347
[116] Buschow K H J 1994 *IEEE Trans. Magn.* **30** 565
[117] Tomida T, Sano N and Uehara M 1997 *J. Appl. Phys.* **81** 7170
[118] Tomida T, Sano N, Hanafusa K, Tomizawa H and Hirosawa S 1999 *Acta Metall.* **47** 875
[119] Nakamura H, Kato K, Sugimoto S, Okada M and Homma M 1998 *Proc. 15th Int. Workshop on Rare Earth Magnets and their Applications (Dresden, Germany, 1988)* vol 1, p 507
[120] Gutfleisch O and Harris I R 1998 *Proc. of 15th Int. Workshop on Rare Earth Magnets and their Applications (Dresden, Germany, 1988)* vol 1, p 487
[121] Gao J, Song X and Wang X 1998 *J. Alloys Comp.* **267** 270
[122] Kubis M, Cao L, Müller K H and Schultz L 1997 *J. Phys. D: Appl. Phys.* **30** L51
[123] Gutfleisch O, Kubis M, Handstein A, Müller K-H and Schultz L 1998 *Appl. Phys. Lett.* **73** 3001
[124] Williamson G K and Hall W H 1953 *Acta Metall.* **1** 22
[125] Bollero A, Kubis M, Gutfleisch O, Müller K H and Schultz L *Acta Metall.* at press
[126] Yeh X L, Samwer K and Johnson W L 1983 *Appl. Phys. Lett.* **42** 242
[127] Müller K-H, Kubis M, Handstein A, Gebel B and Gutfleisch O 2000 *Scr. Mater.* **42** 1013
[128] Coey J M D and Sun H 1990 *J. Magn. Magn. Mater.* **87** L251
[129] Skomski R, Brennan S and Wirth S 1995 *Interstitial Metallic Alloys (NATO-ASI Series E, vol 281)* ed F Grandjean *et al* (Dordrecht: Kluwer) ch 16
[130] Fuji H and Sun H 1995 *Handbook of Magnetic Materials* vol 9 (Amsterdam: Elsevier, North-Holland) ch 3
[131] Wendhausen P A P, Gebel B, Eckert D and Müller K H 1994 *J. Appl. Phys.* **75** 6018
[132] Dempsey N M, Wendhausen P A P, Gebel B, Müller K H and Coey J M D 1996 *Proc. 14th Int. Workshop on Rare Earth Magnets and their Applications (Sao Paolo, Brazil, 1996)* p 349
[133] Shen B G, Kong L S, Wang F W and Cao L 1994 *J. Appl. Phys.* **75** 6253
[134] Shen B G, Wang F W, Kong L S, Cao L and Zhan W S 1993 *Appl. Phys. Lett.* **63** 2288
[135] Cheng Z H, Shen B G, Wang F W, Zhang J X, Gong H Y and Zhao J G 1994 *J. Phys.: Condens. Matter* **6** 1185
[136] Müller K H, Cao L, Dempsey N M and Wendhausen P A P 1996 *J. Appl. Phys.* **79** 5045
[137] Kubis M 2000 *PhD Thesis* Technical University Dresden
[138] Nozieres J P, Perrier de la Bathie R and Gavinet J 1988 *J. Physique* **49** C8 667
[139] Ohki T, Yuri T, Miyagawa M, Takahashi Y, Yoshida C, Kambe S, Higashi M and Itayama K 1989 *Proc. 10th Int. Workshop. on Rare Earth Magnets and their Applications (Kyoto, Japan, 1989)* p 399
[140] Shimoda T, Akioka K, Kobayashi O, Yamagami Y, Ohki T, Miyagawa M and Yuri T 1989 *IEEE Trans. Magn.* **25** 4099
[141] Croat J J 1989 *IEEE Trans. Magn.* **25** 3550
[142] Yoshikawa N, Yamada H, Iwasaki Y, Nagata K and Kasai Y 1994 *Proc. 13th Int. Workshop on Rare Earth Magnets and their Applications (Birmingham, UK, 1994)* p 635
[143] Yoshikawa N, Iriyama T, Yamada H, Kasai Y and Panchanathan V 1999 *IEEE Trans. Magn.* **35** 3268
[144] Grünberger W, Hinz D, Schläfer D and Schultz L 1996 *J. Magn. Magn. Mater.* **157/158** 41
[145] Mishra R K and Lee R W 1986 *Appl. Phys. Lett.* **48** 733
[146] Lee R W, Brewer E G and Schaffel N A 1985 *IEEE Trans. Magn.* **21** 1958
[147] Tenaud P, Chamberod A and Vanoni F 1987 *Solid State Commun.* **63** 303
[148] Luo Y and Graham C D 1989 *Proc. 10th Int. Workshop on Rare Earth Magnets and their Applications (Kyoto, Japan, 1989)* p 427
[149] Li L and Graham C D 1990 *J. Appl. Phys.* **67** 4756
[150] Grünberger W 1998 *Proc. 15th Int. Workshop on Rare Earth Magnets and their Applications (Dresden, Germany, 1998)* p 333
[151] Kirchner A, Hinz D, Panchanathan V, Gutfleisch O, Müller K H and Schultz L *IEEE Trans. Magn.* at press